https://doi.org/10.15407/ujpe71.3.243

Y.M. AZHNIUK,[1] A.I. POGODIN,[2] M.J. FILEP,[1,3] V.V. LOPUSHANSKY,[1] V.M. KRYSHENIK,[1] V.Y. IZAI,[4] L. SATRAPINSKYY,[4] I.M. VOYNAROVYCH,[1] A.V. GOMONNAI[1]

[1] Institute of Electron Physics, Nat. Acad. of Sci. of Ukraine
(21, Universytetska Str., Uzhhorod 88017, Ukraine; e-mail: yu.azhniuk@gmail.com)
[2] Uzhhorod National University
(3, Narodna Sq., Uzhhorod 88000, Ukraine)
[3] Ferenc Rákóczi II Transcarpathian Hungarian Institute
(6 Kossuth Sq., Berehovo 90200, Ukraine)
[4] Centre for Nanotechnology and Advanced Materials, Faculty of Mathematics, Physics and Informatics, Comenius University Bratislava
(Mlynská Dolina, 84248, Bratislava, Slovakia)

STRUCTURAL AND SPECTROSCOPIC STUDY OF UNDOPED AND Ag-DOPED Sb_2S_3 POLYCRYSTALS

Ag-doped Sb_2S_3 polycrystals with silver content up to 10 at.% were obtained by high-temperature synthesis. Chemical composition of the samples determined by EDX spectroscopy corresponds to the element content in the initial mixture with a rather uniform element distribution over the sample surface with slight inhomogeneities of Ag distribution. XRD data confirmed the orthorhombic (stibnite) structure of the synthesized polycrystalline Sb_2S_3 : Ag ingots, for the Ag-containing samples $AgSbS_2$ (β-miargyrite) phase was also revealed. Possible presence of the $AgSbS_2$ phase can also be assumed from Raman measurements performed at low laser power density (P_{exc} = 4 kW/cm^2). Raman spectra at increased P_{exc} (40 kW/cm^2) reveal photostructural and photochemical transformations, namely the formation of Sb_2O_3 and elemental Sb phases due to heating of the sample surface by the tightly focused laser beam.

Keywords: phase-change materials, X-ray diffraction, energy-dispersive X-ray fluorescence spectroscopy, Raman spectroscopy, oxidation.

1. Introduction

Antimony trisulfide (Sb_2S_3) belongs to the class of phase-change materials for high-performance nonvolatile photonics and exists not only in crystalline and amorphous forms, but can also be readily transformed from one form to another by thermal annealing or laser irradiation [1–6]. Upon switching from crystalline to amorphous phase, the band gap of Sb_2S_3 changes from 2.05 to 1.7 eV [7]. Sb_2S_3 is characterized by a high refractive index n, moreover, the difference between the n values in the crystalline and amorphous phases is also quite considerable [8]. An important advantage of Sb_2S_3 compared to traditional phase-change materials (e. g., $Ge_2Sb_2Te_5$), is its very low optical absorption ($k < 10^{-5}$) in the near-infrared and even in the visible spectral range both in the amorphous and crystalline states. This

Citation: Azhniuk Y.M., Pogodin A.I., Filep M.J., Lopushansky V.V., Kryshenik V.M., Izai V.Y., Satrapinskyy L., Voynarovych I.M., Gomonnai A.V. Structural and spectroscopic study of undoped and Ag-doped Sb_2S_3 polycrystals. *Ukr. J. Phys.* **71**, No. 3, 243 (2026). https://doi.org/10.15407/ujpe71.3.243.

enables its application as a medium for building up neural networks, as an alternative to known phase-change materials used in tunable photonic devices [1, 9, 10]. Thermal transport in Sb_2S_3 is dominated by the contribution of phonons rather than by electronic thermal conductivity. This makes it promising for thermoelectric devices [10]. This chalcogenide material has a significant potential for applications in solar energy conversion [4, 5, 11–14].

Needle-shaped Sb_2S_3 (stibnite) crystals at room temperature have an orthorhombic structure (space group *Pbnm*) with unit cell parameters $a = 11.3107$ Å, $b = 3.8363$ Å, $c = 11.2285$ Å [14]. The stibnite structure is formed of long $(Sb_4S_6)_n$ chains (ribbons) along the [001] direction, a single ribbon element consisting of two trigonal SbS_3 and two square SbS_5 pyramids. The ribbons are linked together, forming zigzag-type sheets perpendicular to the (100) plane [14].

Doping Sb_2S_3 with silver is applied, in particular, for films with the intention of decreasing their intrinsic high electrical resistivity that is important for their application as buffer layers in photovoltaics as well as of increasing their refractive index thereby making them attractive for applications in photonics [15]. A quite efficient method to introduce silver into Sb_2S_3 is photodoping, or optically induced diffusion and dissolution when a thin layer of Ag is deposited onto the sample and subsequently illuminated to enhance its diffusion into Sb_2S_3, thereby achieving the desirable silver content [16]. Sb_2S_3-based materials with incorporated silver are promising for application in rechargeable lithium-ion batteries, mostly as alternatives for the existing anode materials [17]. In such a case, the presence of silver accelerates electrochemical processes in the batteries, increases their lifetime and charging speed as well as reduces the battery resistance [17].

Here we present the results of our study of polycrystalline Sb_2S_3 and $Sb_2S_3:Ag$ ingots by X-ray diffraction (XRD), energy-dispersive X-ray fluorescence spectroscopy (EDX), and Raman spectroscopy.

2. Experimental

Sb_2S_3 was synthesized from high-purity elemental Sb (99.999%) and S (99.9995%) taken in stoichiometric proportions in evacuated quartz ampoules by a two-temperature synthesis with the "hot" (Sb-containing) zone temperature of 650 °C. While the interaction between the components was going on, the ampoule was gradually moved to the "hot" zone and after the interaction being finished it was cooled down to room temperature at a rate 50 K/h. Colloidal silver was obtained by reduction of AgCl by hydrazine chloride $N_2H_6Cl_2$ in an alkaline medium (NaOH). AgCl was obtained from $AgNO_3$ and KCl dissolved in deionized water. Purity of $AgNO_3$, KCl, $N_2H_6Cl_2$, and NaOH was not worse than 99.95%.

$Sb_2S_3:Ag$ samples were synthesized from Sb_2S_3 and colloidal Ag in evacuated quartz ampoules at 650 °C. The melts were kept at this temperature under constant stirring for 4 h and subsequently quenched in air.

The polycrystalline Sb_2S_3 and $Sb_2S_3:Ag$ samples were studied by X-ray diffraction (XRD) using an AXRD benchtop diffractometer with Cu K_α radiation and a Ni filter. The chemical composition of the samples was analysed based on the EDX data obtained using a Tescan Vega TS5136MM scanning electron microscope equipped with an Oxford Instruments INCAx-act EDX detector (129 eV resolution at 5.9 keV). A thin (15–20 nm) film of amorphous carbon was sputter-deposited on the surface of the samples to avoid surface charging during measurement of the spectra and EDX mapping. The primary electron beam energy of 20 keV was used for the elemental analysis. The EDX mapping was performed at a primary electron beam energy of 10 keV.

Micro-Raman spectra of the polycrystalline Sb_2S_3 and $Sb_2S_3:Ag$ samples were measured at room temperature using an XPloRa Plus spectrometer (Horiba) equipped with a 532 nm laser and a cooled CCD camera.

3. Results and Discussion

XRD patterns of the polycrystalline $Sb_2S_3:Ag$ ingots are shown in Fig. 1. At a first glance, the diffractograms look quite similar for all the samples (Fig. 1, *a*), exhibiting a strong similarity to the reference data for the orthorhombic stibnite structure (PDF 42-1393 [18]). However, a more careful look into the narrower range between 25° and 35° (see the zoomed-in view in Fig. 1, *b*) shows diffraction peaks at 27.3° and 31.6° emerging already at the lowest silver content (0.02) and increasing in intensity with increasing silver content. These features perfectly match reflections from (111) and (200)

planes of the cubic structure of $AgSbS_2$ (β-miargyrite) [19, 20], the reference curve being shown in Fig. 1, *b* for convenience along with the experimental data. It may be concluded that in our case polycrystalline $Sb_2S_3 : Ag$ samples with $x > 0$ contain $AgSbS_2$ phase as well. Note that earlier crystallization of cubic $AgSbS_2$ was reported (along with that of stibnite) for amorphous $Ag_x(Sb_{0.33}S_{0.67})_{100-x}$ samples illuminated by a 514.5 nm laser light [16, 21] while for $Ag_x(Sb_{0.4}S_{0.6})_{100-x}$ samples with Sb-to-S ratio similar to ours, photoinduced crystallization of rhombohedral Ag_3SbS_3 (pyrargyrite) was observed [21].

The content of the Sb_2S_3 and $AgSbS_2$ phases in the obtained alloys was quantitatively estimated using the Rietveld refinement method with the PowderCell2.4 software [22]. The obtained data are summarized in Table 1 showing a relatively good agreement between the Ag content in the initial mixture and the XRD-based data. A slight deviation is probably due to the small number of the observed reflections corresponding to cubic $AgSbS_2$ as well as to the overlap of diffraction peaks at 31.6° and 45.4° for both phases. Since the $AgSbS_2$ phase content obtained using the Rietveld method is only slightly lower than the theoretically calculated value, combined with the absence of diffraction peaks of other phases, it can be concluded that most of the silver atoms entered into the composition of the formed $AgSbS_2$ phase. Note that synthesis, properties, and applications of $AgSbS_2$ which is a promising material for photovoltaics are studied in detail in recent publications [23–25] and references therein.

EDX spectra measured for the Sb_2S_3:Ag samples (Fig. 2) confirmed the presence of silver, antimony, and sulphur. The inset in the figure shows that the element content is in good agreement with the content loaded in the initial mixture.

Table 1. **Content of the $AgSbS_2$ phase *y* in $Sb_2S_3 : Ag$ samples obtained from XRD data using Rietveld refinement versus the content of Ag in the initial mixture *x***

x, mol. %	*y*, mass %	*y*, mol. %
2	1.25	1.44
4	2.54	2.93
6	3.69	4.24
8	5.33	6.11
10	8.31	9.49

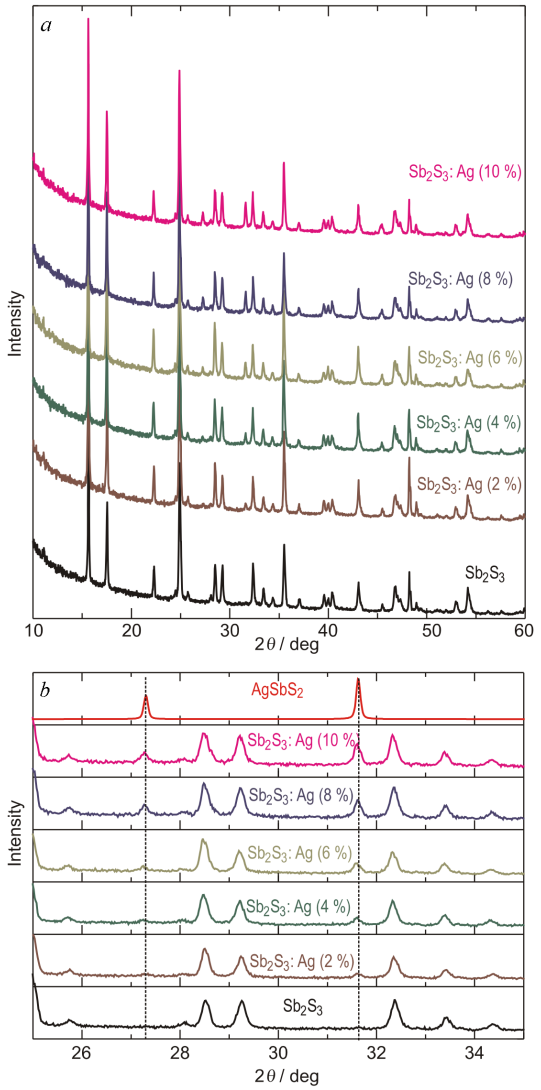

Fig. 1. XRD patterns of polycrystalline $Sb_2S_3 : Ag$ samples (*a*) and a zoomed-in view of the same XRD patterns in a narrower range (*b*) along with the reference $AgSbS_2$ diffractogram adapted from [19]

EDX mapping of the samples under investigation was performed to check the uniformity of the element distribution. Examples of the element maps, along with the scanning electron microscopy (SEM) image of the mapped area, are shown in Fig. 3. They revealed relatively homogeneous patterns over the scanned surface area for the elements of interest, with some areas of increased silver content, seemingly along the "steps" on the polycrystalline sample surface.

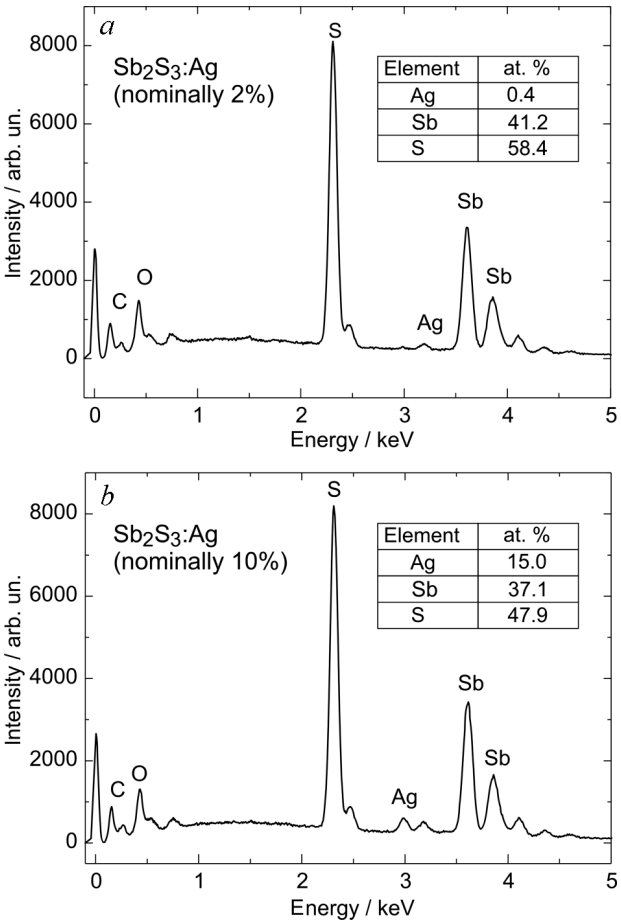

Fig. 2. EDX spectra of polycrystalline $Sb_2S_3:Ag$ samples. The insets show the element content calculated from the spectra

The Raman spectrum of a bulk polycrystalline Sb_2S_3 sample measured at the excitation with a low $P_{exc} = 4$ kW/cm^2, is shown in Fig. 4. It is well known from group-theoretical analysis that the phonon spectrum of Sb_2S_3 includes in total 30 Raman-active modes ($10A_g + 5B_{1g} + 10B_{2g} + 5B_{3g}$) [3, 26, 27]. The most detailed recent polarized Raman study performed on Sb_2S_3 single crystals (stibnite) and polycrystals using multiple excitation wavelengths and low temperatures as well as comparison with the calculation data claims symmetry assignment and identification of all 30 modes, although some of them are not observed as distinct peaks, but can be identified after deconvolution of the experimental spectra [27]. Our measurements, performed for polycrystalline samples, reveal a less extensive set of features, similar to those observed earlier by other groups for bulk [26, 28–30] and thin-film [3, 15, 18, 31–34] polycrystalline Sb_2S_3.

As can be seen from Fig. 4, the most pronounced peaks are the higher-frequency ones, with maxima in the range from 280 to 311 cm^{-1}. Interestingly, two Raman spectra of the same polycrystalline Sb_2S_3 sample measured under similar conditions at different spots on the sample surface exhibit the higher-frequency maximum at quite different frequency positions, 302 and 311 cm^{-1} (see the two bottom curves in Fig. 4). Likewise, Raman studies of Sb_2S_3 polycrystals by other authors also reported the highest-frequency peak at 303–305 cm^{-1} [3, 29, 30, 32] or at 310–312 cm^{-1} [18,27,33]. Moreover, in an earlier publication [26], three distinct features were revealed for Sb_2S_3 in this spectral range, being even more pronounced at low-temperature measurements.

The peak at 281 cm^{-1} is assigned to A_g symmetry [3, 15, 18, 26, 32, 34]. However, opinions on the assignment of the maximum at 303–305 cm^{-1} vary: some authors relate it to A_g symmetry vibration [3, 26] while others ascribe it to B_{1g} [32]. Opinions on the assignment of the highest-frequency peak at 310–312 cm^{-1} are also different: it is considered an A_g symmetry vibration [27, 33, 34], a B_g [3, 15] or a B_{2g} [26] symmetry one. Our measurements were unpolarized, and the samples were polycrystalline; hence we have no own experimental data to rely on for the symmetry assignment, however, in our opinion, the conclusions of [27] seem more trustworthy since they are based on their own polarized spectra measured for a single crystal at multiple wavelengths and are supported by their calculations.

In our measurements for Sb_2S_3 the two higher-frequency bands above 300 cm^{-1} are not resolved, one of them being more intense while the other is masked by the more pronounced band. Since the experiment was carried out for polycrystalline samples, different preferred orientations of crystallites in the probed volume of the sample can be the reason for the observed discrepancies in intensities and even in the number of the Sb_2S_3 bands revealed in this spectral range.

As noted above, the crystalline structure of Sb_2S_3 contains pyramidal units of two types, namely, SbS_3 and SbS_5 [3, 14]. The Raman features at 280–282 cm^{-1} and 303–305 cm^{-1} are ascribed to antisymmetric stretching vibrations of Sb–S bonds [18]. In a

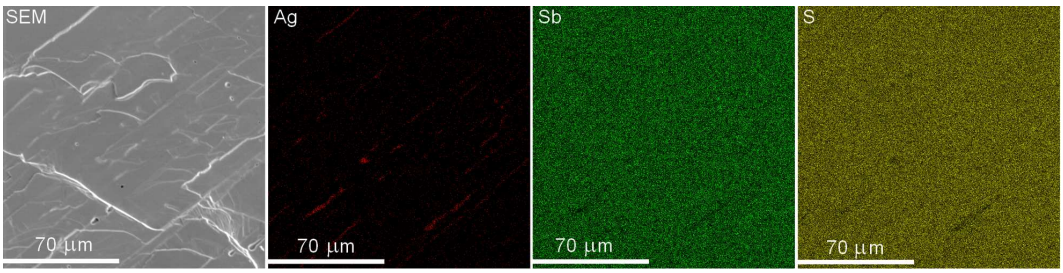

Fig. 3. Scanning electron microscopy (SEM) image and EDX-based maps of element (Ag, Sb, and S) content distribution for the Sb_2S_3 : Ag sample with 2 at.% Ag

recent paper [3], the lower-frequency band is related to the Sb–S bond vibration in trigonal SbS_3 pyramids while the higher-frequency peak is related to that in SbS_5 units. Such an assignment seems quite reasonable since bond lengths in SbS_3 and SbS_5 pyramidal units are slightly different because of different coordination environment [14]. The highest-frequency peak at 311 cm^{-1} corresponds to symmetric stretching vibrations of Sb–S bonds [18, 33].

Lower-frequency features, which are less pronounced, nevertheless clearly correlate with the data of earlier studies and are assigned to A_g (155 cm^{-1}) [3, 15, 33, 34], A_g (190 cm^{-1}) [3, 15, 26, 33], and B_{1g}/B_{3g} (237 cm^{-1}) [3,15,26,33,34] symmetry vibrations. Exceptionally, the 190 cm^{-1} band is attributed to B_{2g} symmetry by the authors of Ref. [34].

Adding silver to the sample composition in the amount up to 10 at.% does not lead to striking changes in the Raman spectra (see Fig. 4). As the XRD data give clear evidence for the presence of $AgSbS_2$ crystallites in the silver-containing samples, one could expect characteristic $AgSbS_2$ Raman bands to appear with increasing Ag content. In fact, in the spectrum of the Sb_2S_3 : Ag sample with 10 at.% Ag one can observe a weak feature at 254 cm^{-1}, the intensity of which only slightly exceeds the noise level. This frequency corresponds to the most pronounced Raman peaks of miargyrite at 250 cm^{-1} [35] or cuboargyrite at 254 cm^{-1} [15] (monoclinic and cubic modifications of $AgSbS_2$, respectively). One can claim that, even in spite of the weak intensity, the presence of the discussed feature in the Raman spectrum of Sb_2S_3 : Ag (10 at.% Ag) supports the conclusion regarding the existence of a crystalline $AgSbS_2$ phase in the samples based on the XRD data (Fig. 1, *b*) which is in itself quite convincing. Alternatively, one may assume that the weak maximum at 254 cm^{-1} can be a signature of antimony oxide Sb_2O_3 which is known to possess an intense Raman feature at this frequency [38]. However, contrary to $AgSbS_2$, the XRD measurements did not confirm the presence of Sb_2O_3 phase in the sample (Fig. 1).

Raman spectra of Sb_2S_3:Ag polycrystals measured at a higher $P_{exc} = 40$ kW/cm^2 (Fig. 5), however, are drastically different from those obtained at a lower P_{exc}. New intense peaks are observed in all samples near 104, 115, 146, 187, 249, 367, and 446 cm^{-1}. These features are revealed in the spectra of all samples, independent of the silver content, being much more intense than the most pronounced Sb_2S_3 maxima observed at a lower P_{exc}, which in this case are seen as a rather smeared background at 280–300 cm^{-1}. Only in the undoped Sb_2S_3 sample one can clearly observe the two maxima at 275 and 295 cm^{-1} (slightly shifted downward with respect to the low-P_{exc} measurements) in this spectral range.

Spectral positions and intensities of most of the newly emerged peaks remarkably coincide with the values for senarmontite, a cubic modification of Sb_2O_3. Technically, one can relate the peak at ∼187 cm^{-1} to polycrystalline Sb_2S_3, since the spectrum of the latter at a low P_{exc} contains a weak feature at a close frequency (see Fig. 4). However, the intensity of the ∼187 cm^{-1} peak, much higher than those of the higher-frequency peaks (generally the most prominent for Sb_2S_3), suggests that the feature is related to a different phase, namely Sb_2O_3, which can be formed on the Sb_2S_3 surface under laser irradiation.

It should be noted that the spectral position of the intense Raman peak at 249–250 cm^{-1}, emerging in the spectra of Sb_2S_3 : Ag polycrystals measured at $P_{exc} = 40$ kW/cm^2, coincides with that of the dominating feature reported at 250 cm^{-1} for crys-

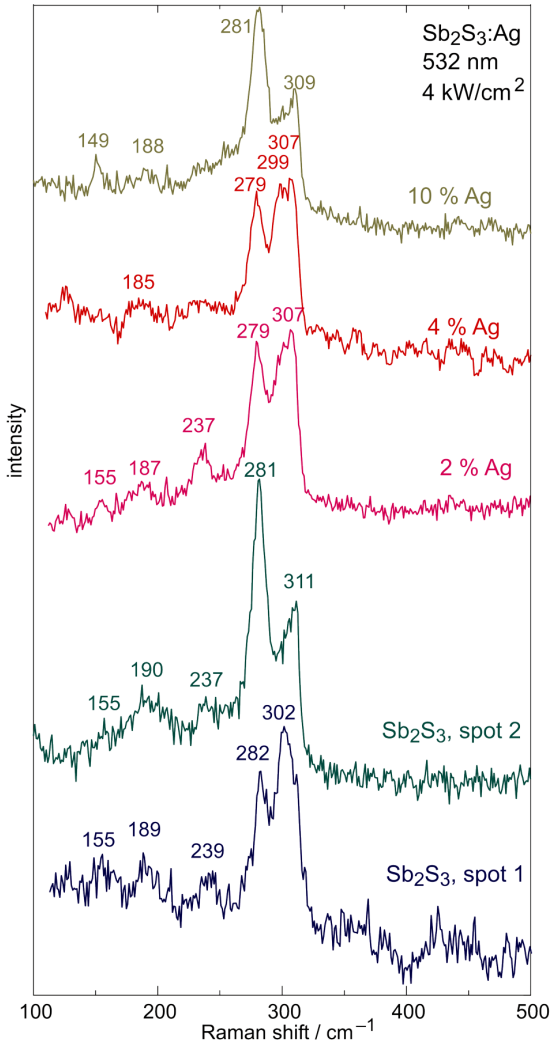

Fig. 4. Raman spectra of bulk polycrystalline $Sb_2S_3:Ag$ samples measured at the excitation with $\lambda_{exc} = 532$ nm and $P_{exc} = 4$ kW/cm^2. Two spectra presented for the Sb_2S_3 sample measured from two different spots demonstrate the diversity related to the sample polycrystallinity

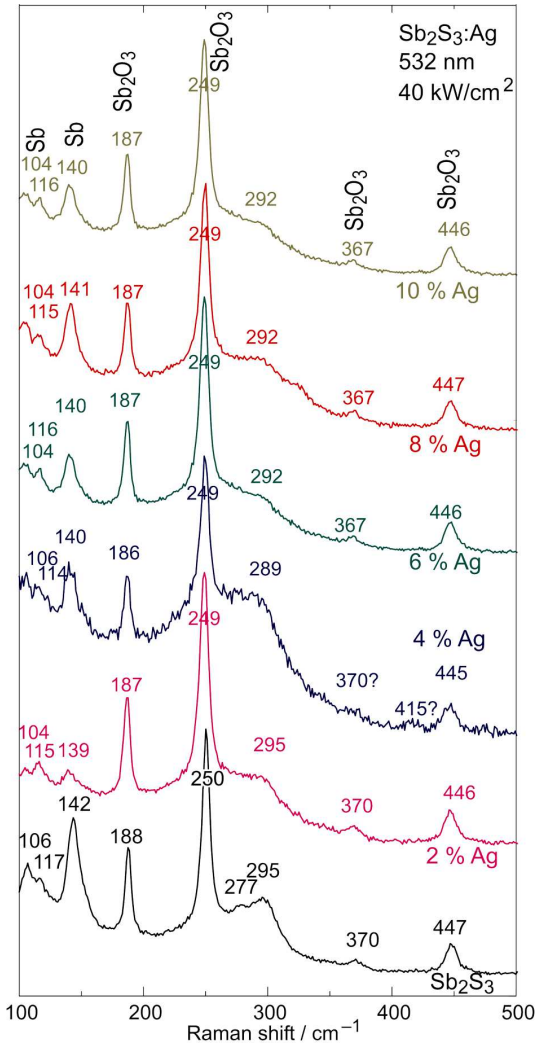

Fig. 5. Raman spectra of bulk polycrystalline $Sb_2S_3:Ag$ samples measured at the excitation with $\lambda_{exc} = 532$ nm and $P_{exc} = 40$ kW/cm^2

talline $AgSbS_2$ (miargyrite) [35]. Therefore, one may be tempted to assume that possible photoinduced formation of $AgSbS_2$ crystallites also contributes to the high intensity of the discussed peak at 249–250 cm^{-1}. A careful look at the intensity ratio of the emerging ∼250 cm^{-1} and ∼187 cm^{-1} peaks would not clarify the issue in this case since this ratio in the spectra of Sb_2O_3 [29] and $AgSbS_2$ [35] appears quite similar. Hence, the observed independence of the discussed ratio on the silver content in the samples (Fig. 5) does not provide any clarification without further studies. Note that the appearance of the $AgSbS_2$ phase upon annealing was assumed in an earlier study [15] based on the emerging ∼250 cm^{-1} peak, however, in our opinion, such an explanation is not sufficiently substantiated since, similar to our case, this feature can equally result from Sb_2O_3 formed due to thermal oxidation. Meanwhile, annealing of amorphous Ag–Sb–S films with much higher silver content than that in our case clearly showed the formation of cubic and monoclinic $AgSbS_2$, as well as monoclinic and hexagonal Ag_3SbS_3 phases [36].

The lower-frequency features near 115 and 150 cm^{-1}, on the contrary, are not observed for Sb_2O_3, but are typically assigned to elemental antimony [29] which is known to possess E_g and A_{1g} modes, respectively, at these frequencies [37].

Evidently, Raman fingerprints of Sb_2O_3 and elemental Sb (as well as possibly $AgSbS_2$) can arise in the spectra of the samples due to photochemical reactions on their surface initiated, first of all, by local heating of the sample in the laser spot [29]. The reaction occurs within first seconds after the onset of illumination. From the spectrum of the Sb_2O_3-related features one may conclude that oxidation of the sample surface leads to the formation of cubic senarmontite, not its orthorhombic isomorph valentinite which has a quite different set of Raman peaks [38, 39], or another antimony oxide Sb_2O_4 (cervantite) with the strongest peak near 200 cm^{-1} [38]. However, the possibility of formation of valentinite should not be completely excluded since the most intense feature of the latter is reported at 142–143 cm^{-1} [38, 39]; hence it, along with the A_{1g} vibration of elemental Sb, can contribute to the maximum observed in Fig. 5 at 139–142 cm^{-1}. Here one should keep in mind that the mentioned literature data refer to room temperature, however, in our case, due to the local heating of the sample by the above-bandgap laser light, the actual Raman frequencies are expected to be somewhat lower. Hence, the feature observed at 139–142 cm^{-1} (Fig. 5) due to the increased temperature in the laser spot, is quite likely to correspond to the A_{1g}-type vibration of elemental Sb reported at room temperature at 150 cm^{-1} [37]. Note that the Raman spectra measured at $P_{exc} = 40$ kW/cm^2, are similar for all samples under study, independent of the silver content.

Note that Raman features of elemental Sb and Sb_2O_3 were also revealed at elevated P_{exc} in an earlier study of Sb_2S_3 by other authors [29]. The effect of photooxidation of Sb_2S_3 is an important issue leading to the degradation of Sb_2S_3-based optical phase-change materials; therefore, in order to prevent it, Sb_2S_3 films can be passivated by ZnS/SiO_2 layers [34].

In the Raman experiment, after the sample having been subjected to 532 nm laser illumination at $P_{exc} = 40$ kW/cm^2 initiating the above photochemical transformations, we performed one more Raman measurement from the same spot on the surface at a reduced $P_{exc} = 4$ kW/cm^2 (Fig. 6). One can clearly see that the Sb- and Sb_2O_3-related features remain in the spectra, showing that the oxidation effects on the sample surface are irreversible. It is clearly seen that the spectral positions of the Sb- and Sb_2O_3-related peaks are slightly higher than those measured at $P_{exc} = 40$ kW/cm^2, thereby showing the difference between the temperatures attained due to the sample heating by the laser beam at different P_{exc} values.

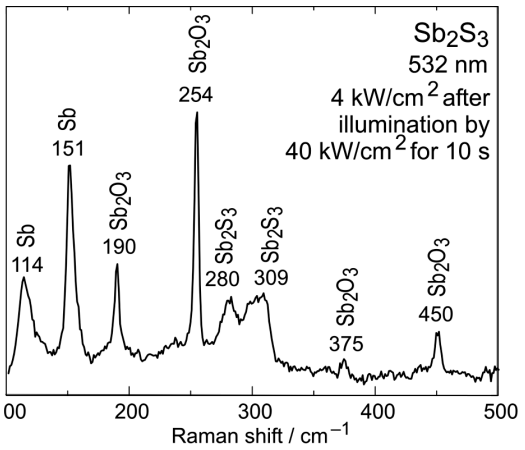

Fig. 6. Raman spectra of bulk polycrystalline Sb_2S_3 measured at the excitation with $\lambda_{exc} = 532$ nm and at $P_{exc} = 4$ kW/cm^2 measured from the same spot on the sample surface after the measurement at $\lambda_{exc} = 532$ nm and at $P_{exc} = 40$ kW/cm^2

Although the thermal effect of the laser illumination during the Raman measurement is generally considered the most essential mechanism of the photochemical and photostructural transformations on the Sb_2S_3 : Ag sample surface, one should also mention the possibility of a nonthermal mechanism of photoinduced changes. In particular, it is known to be responsible for photosoftening of amorphous arsenic chalcogenides resulting in the formation of nanocrystals with the participation of dopant atoms [40, 41] and for Sb_2S_3 and Sb_2S_3 : Ag one should likewise consider the possibility of nonthermal effects resulting in the observed photochemical transformations. In an attempt to at least partly separate the thermal and nonthermal effects, we performed Raman measurements of the polycrystalline Sb_2S_3 sample immersed in isopropanol to provide essential heat dissipation from the measurement area as well as to eliminate access of ambient air to the sample surface. We assumed that this would reduce the thermal effect of the incident light on the sample surface and pre-

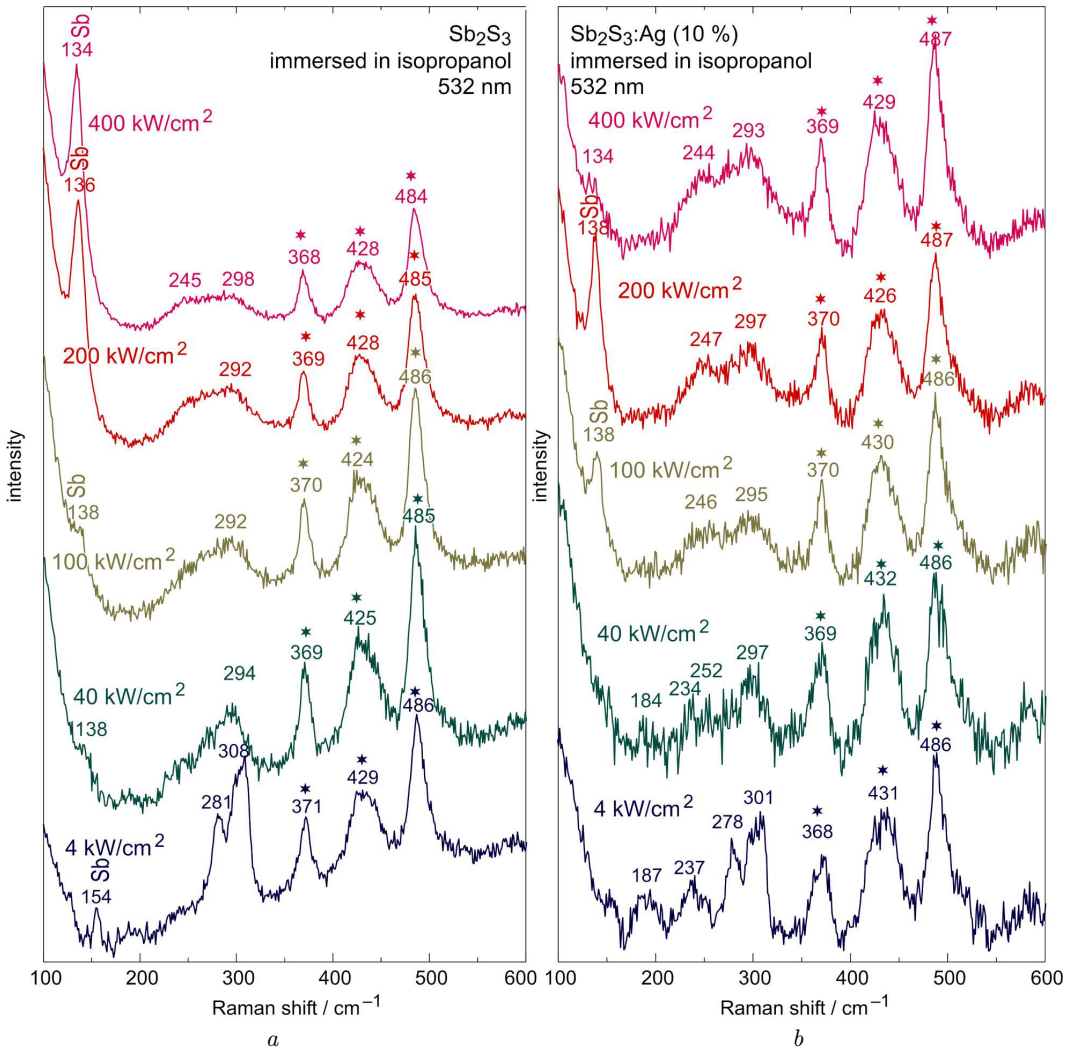

Fig. 7. Raman spectra of bulk polycrystalline Sb_2S_3 (*a*) and Sb_2S_3 : Ag (10 at.%) (*b*) immersed in isopropanol measured at the excitation with $\lambda_{exc} = 532$ nm and various P_{exc} values. The isopropanol peaks are marked by asterisks

vent (or at least hinder) the surface oxidation in the laser spot.

Raman spectra of the Sb_2S_3 and Sb_2S_3 : Ag (10 at.%) samples immersed in isopropanol are shown in Fig. 7. It is clearly seen from the figure that at P_{exc} up to 400 kW/cm^2 no features related to Sb_2O_3 are revealed which means that in this case photooxidation does not occur on the sample surface under laser illumination. Evidently, liquid isopropanol not only dissipates heat from the sample surface, but, which in this case seems more important, blocks supply of oxygen from the ambient air thereby preventing oxidation. However, a rather weak feature at 138 cm^{-1}, related, as noted above, to elemental Sb, appears already at $P_{exc} = 40$ kW/cm^2 and noticeably increases in intensity with P_{exc}, becoming the dominating peak in the spectrum at $P_{exc} = 200$ kW/cm^2. As the Sb_2S_3 decomposition under laser irradiation is most likely due to a thermal mechanism, one can assume that dissipation of heat from the laser spot by liquid isopropanol is insufficient to prevent this reaction at high P_{exc} values.

It seems important to note that the choice of isopropanol as a liquid used to isolate the Sb_2S_3 sam-

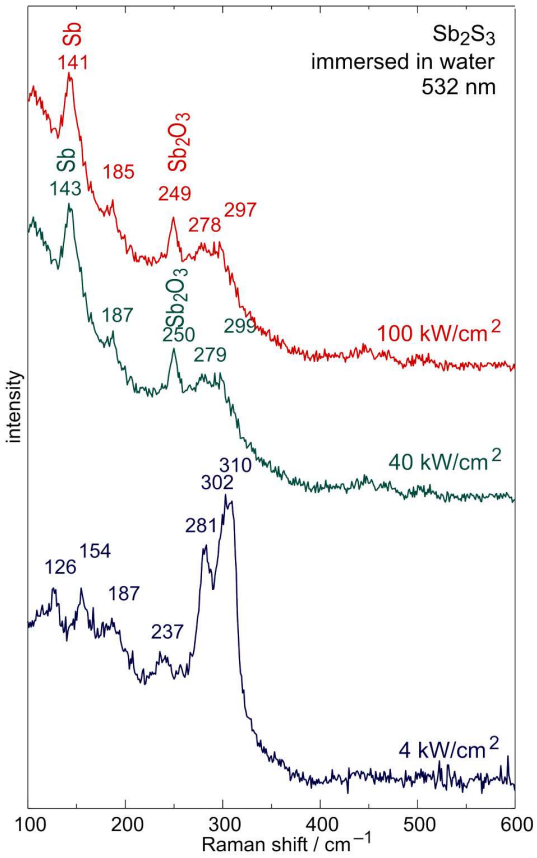

Fig. 8. Raman spectra of bulk polycrystalline Sb_2S_3 immersed in water measured at the excitation with $\lambda_{exc} = 532$ nm and various P_{exc} values

ple surface from ambient oxygen is quite reasonable not only due to the absence of intense Raman peaks directly in the spectral range of interest (which is not the case, for instance, for toluene), but also due to the above-mentioned non-reactivity of isopropanol. For instance, Raman spectra of the Sb_2S_3 sample immersed in deionized water measured at $P_{exc} \geq 40$ kW/cm^2 clearly show the appearance of a Sb_2O_3-related feature near 250 cm^{-1} evidently due to the photochemical reaction of antimony atoms with oxygen released from the water (Fig. 8).

4. Conclusions

Sb_2S_3 : Ag polycrystals with silver content up to 10 at.% were obtained by high-temperature synthesis. Chemical composition of the samples determined by EDX spectroscopy corresponds to the element content in the initial mixture. The element distribution over the samples measured by the EDX mapping is rather uniform with slight inhomogeneities in the silver distribution. XRD data confirmed the orthorhombic (stibnite) structure of the synthesized polycrystalline Sb_2S_3:Ag ingots, the Ag-containing samples exhibiting the presence of the $AgSbS_2$ (β-miargyrite) phase as well.

Raman spectroscopy data measured at low laser power density ($P_{exc} = 4$ kW/cm^2) suggest possible (although not unambiguous) presence of the $AgSbS_2$ phase, thereby supporting the XRD data. Raman measurements at increased P_{exc} (40 kW/cm^2) revealed photostructural and photochemical transformations, namely the formation of Sb_2O_3 and elemental Sb phases due to heating of the sample surface by the tightly focused laser light. Raman measurements performed for the samples immersed in liquid isopropanol prevent the sample oxidation by blocking access of air to the laser spot, hence, contrary to measurements in air, no features of Sb_2O_3 are observed in the Raman spectra measured at elevated P_{exc}. The observed tendency of the material towards the surface oxidation under laser light indicates that surface passivation should be considered during the fabrication of Sb_2S_3 thin film-based optical phase-change elements.

This work was supported by the "Advanced Science in Ukraine" grant No. 2023.03/0013 from National Research Foundation of Ukraine.

1. W. Dong, H. Liu, J.K. Behera, L. Lu, R.J.H. Ng, K.V. Sreekanth, X. Zhou, J.K.W. Yang, R.E. Simpson. Wide bandgap phase change material tuned visible photonics. *Adv. Funct. Mater.* **29**, 1806181 (2018).
2. M. Xu, R. Gu, C. Qiao, H. Tong, X. Cheng, C.-Z. Wang, K.-M. Ho, S. Wang, X. Miao, M. Xu. Unraveling the structural and bonding nature of antimony sesquichalcogenide glass for electronic and photonic applications. *J. Mater. Chem. C* **9**, 8057 (2021).
3. Y. Gutiérrez, A.P. Ovvyan, G. Santos, D. Juan, S.A. Rosales, J. Junquera, P. García-Fernández, S. Dicorato, M.M. Giangregorio, E. Dilonardo, F. Palumbo, M. Modreanu, J. Resl, O. Ishchenko, G. Garry, T. Jonuzi, M. Georghe, C. Cobianu, K. Hingerl, C. Cobet, F. Moreno, W.H.P. Pernice, M. Losurdo. Interlaboratory study on Sb_2S_3 interplay between structure, dielectric function, and amorphous-to-crystalline phase change for photonics. *iScience* **25**, 104377 (2022).
4. S. Barthwal, S. Singh, A.K. Chauhan, N.S. Prabhu, A.G. Prabhudessai, K. Ramesh. A comprehensive insight

into deep-level defect engineering in antimony chalcogenide solar cells. *Mater. Adv.* **4**, 5998 (2023).
5. M.A. Farhana, A. Manjceevan, J. Bandara. Recent advances and new research trends in Sb_2S_3 thin film based solar cells. *J. Sci.: Adv. Mater. Devices* **8**, 141 (2023).
6. C. Laprais, C. Zrounba, J. Bouvier, N. Blanchard, M. Bugnet, A. Gassenq, Y. Gutiérrez, S. Vazquez-Miranda, S. Espinoza, P. Thiesen, R. Bourrellier, A. Benamrouche, N. Baboux, G. Saint-Girons, L. Berguiga, S. Cueff. Reversible single-pulse laser-induced phase change of Sb_2S_3 thin films: multi-physics modeling and experimental demonstrations. *Adv. Opt. Mater.* **12**, 2401214 (2024).
7. A. Mandal, Y. Cui, L. McRae, B. Gholipour. Reconfigurable chalcogenide phase change metamaterials: A material, device, and fabrication perspective. *J. Phys.: Photonics* **3**, 022005 (2021).
8. J. Faneca, I. Zeimpekis, S.T. Ilie, T.D. Bucio, K. Grabska, D.W. Hewak, F.Y. Gardes. Towards low loss non-volatile phase change materials in mid index waveguides. *Neuromorph. Comput. Eng.* **1**, 014004 (2021).
9. Z. Fang, J. Zheng, A. Saxena, J. Whitehead, Y. Chen, A. Majumdar. Non-volatile reconfigurable integrated photonics enabled by broadband low-loss phase change material. *Adv. Opt. Mater.* **9**, 2002049 (2021).
10. K. Aryana, H.J. Kim, M.R. Islam, N. Hong, C.C. Popescu, S. Makarem, T. Gu, J. Hu, P.E. Hopkins. Optical and thermal properties of $Ge_2Sb_2Te_5$, Sb_2S_3, and Sb_2Se_3 for reconfigurable photonic devices. *Opt. Mater. Expr.* **13**, 3277 (2023).
11. S. Messina, M.T.S. Nair, P.K. Nair. Solar cells with Sb_2S_3 absorber films. *Thin Solid Films* **517**, 1759 (2009).
12. K.F. Abd-El-Rahman, A.A.A. Darwish. Fabrication and electrical characterization of p-Sb_2S_3/n-Si heterojunctions for solar cells application. *Curr. Appl. Phys.* **11**, 1265 (2011).
13. J. Escorcia-Garcia, D. Becerra, M.T.S. Nair, P.K. Nair. Heterojunction CdS/Sb_2S_3 solar cells using antimony sulfide thin films prepared by thermal evaporation. *Thin Solid Films* **569**, 28 (2014).
14. R. Kondrotas, C. Chen, J. Tang. Sb_2S_3 solar cells. *Joule* **2**, 857 (2018).
15. C.J. Diliegros-Godines, J. Santos Cruz, N.R. Mathews, M. Pal. Effect of Ag doping on structural, optical and electrical properties of antimony sulfide thin films. *J. Mater. Sci.* **53**, 11562 (2018).
16. J. Gutwirth, T. Wágner, P. Bezdička, Mil. Vlček, S.O. Kasap, M. Frumar. Influence of silver concentration in $Ag_x(Sb_{0.33}S_{0.67})_{100-x}$ thin amorphous films on photoinduced crystallization. *J. Non-Cryst. Solids* **353**, 1431 (2007).
17. S.F. Ho, Y.C. Yang, H.Y. Tuan. Silver boosts ultra-long cycle life for metal sulfide lithium-ion battery anodes: Taking $AgSbS_2$ nanowires as an example. *J. Colloid Interf. Sci.* **621**, 416 (2022).
18. M.I. Medina-Montes, Z. Montiel-González, F. Paraguay-Delgado, N.R. Mathews, X. Mathew. Structural, morphological and spectroscopic ellipsometry studies on sputter deposited Sb_2S_3 thin films. *J. Mater. Sci.: Mater. Electron.* **27**, 9710 (2016).
19. S. Geller, J.H. Wernick. Ternary semiconducting compounds with sodium chloride-like structure: $AgSbSe_2$, $AgSbTe_2$, $AgBiS_2$, $AgBiSe_2$. *Acta Crystallogr.* **12**, 46 (1959).
20. B. Zhou, M. Li, Y. Wu, C. Yang, W.-H. Zhang, C. Li. Monodisperse $AgSbS_2$ nanocrystals: Size-control strategy, large-scale synthesis, and photoelectrochemistry. *Chem. Eur. J.* **21**, 11143 (2015).
21. J. Gutwirth, T. Wágner, M. Frumar, P. Bezdička, Mil. Vlček. XRD study of laser induced crystallisation of (Ag)–Sb–S amorphous thin films prepared by thermal evaporation combined with optically induced diffusion and dissolution of Ag. *Phys. Chem. Glasses: Eur. J. Glass Sci. Technol. B* **47**, 229 (2006).
22. W. Kraus, G. Nolze. POWDER CELL – a program for the representation and manipulation of crystal structures and calculation of the resulting X-ray powder patterns. *J. Appl. Cryst.* **29**, 301 (1996).
23. U. Chalapathi, A.S. Reddy, P.R. Prasad, G. Manjula, S. Sangaraju, R. Cheruku, B.A. Al-Asbahi, S. Alhammadi, C.P. Reddy, K. Mohanarangam, B.P. Reddy, S.-H. Park. Two-stage-processed $AgSbS_2$ films for thin-film solar cells. *Mater. Sci. Semicond. Proc.* **168**, 107821 (2023).
24. V. Ekanayake, M.F. Webster, M. Dhillon, D.A. Kunar, S. Nagorny, M. Turfanda, M.P. Lewis, P.L. Wang. Crystal growth of α-$AgSbS_2$ and its preliminary characterization for radiation detector applications. *Cryst. Eng. Comm.* **27**, 4258 (2025).
25. E. Dutková, M. Baláž, J. Kováč, M.J. Sayagués, M. Wohlgemuth, Z. Lukáčová Bujňáková, L. Findoráková, J. Kováč Jr., S. Kováčová, M. Marton, P. Jacko, M. Bereš. Rapid one-step mechanochemical synthesis of ternary semiconductor $AgSbS_2$ for photovoltaic applications. *J. Mater. Sci.* **60**, 14605 (2025).
26. Y.A. Sorb, V. Rajaji, P.S. Malavi, U. Subbarao, P. Halappa, S.C. Peter, S. Karmakar, C. Narayana. Pressure-induced electronic topological transition in Sb_2S_3. *J. Phys.: Condens. Matter* **28**, 015602 (2016).
27. V. Rotaru, P. Vidal-Fuentes, X. Alcobe, T. Jawhari, A. López-García, A. Pérez-Rodríguez, I. Becerril-Romero, V. Izquierdo-Roca, M. Guc. Practical methodologies for accelerated research and application of this low dimensional material. *iScience* **27**, 109619 (2024).
28. J.P. Tiwari, K. Shahi. Mechanochemically synthesized Ag_2S–Sb_2S_3 amorphous fast ionic conductors. *Mater. Sci. Eng. B* **141**, 8 (2007).
29. P. Makreski, G. Petruševski, S. Ugarković, G. Jovanovski. Laser-induced transformation of stibnite (Sb_2S_3) and other structurally related salts. *Vibr. Spectrosc.* **68**, 177 (2013).
30. A.V. Kozytskiy, O.L. Stroyuk, M.A. Skoryk, V.M. Dzhagan, S.Ya. Kuchmiy, D.R.T. Zahn. Photochemical formation and photoelectrochemical properties of TiO_2/Sb_2S_3

heterostructures. *J. Photochem. Photobiol. A* **303–304**, 8 (2015).
31. I. Watanabe, S. Noguchi, T. Shimizu. Study on local structure in amorphous Sb–S films by Raman scattering. *J. Non-Cryst. Solids* **58**, 35 (1983).
32. S. Shaji, L.V. Garcia, S.L. Loredo, B. Krishnan, J.A. Aguilar Martinez, T.K. Das Roy, D.A. Avellaneda. Antimony sulfide thin films prepared by laser assisted chemical bath deposition. *Appl. Surf. Sci.* **393**, 369 (2017).
33. R. Parize, T. Cossuet, O. Chaix-Pluchery, H. Roussel, E. Appert, V. Consonni. In situ analysis of the crystallization process of Sb_2S_3 thin films by Raman scattering and X-ray diffraction. *Mater. Design* **121**, 1 (2017).
34. M. Delaney, I. Zeimpekis, D. Lawson, D.W. Hewak, O.L. Muskens. A new family of ultralow loss reversible phase-change materials for photonic integrated circuits: Sb_2S_3 and Sb_2Se_3. *Adv. Funct. Mater.* **30**, 2002447 (2020).
35. B. Minceva-Sukarova, G. Jovanovski, P. Makreski, B. Soptrajanov, W. Griffith, R. Willis, I. Grzetic. Vibrational spectra of $M^IM^{III}S_2$ type synthetic minerals (M^I = Tl or Ag and M^{III} = As or Sb). *J. Mol. Struct.* **651–653**, 181 (2003).
36. M.I. Medina-Montes, L.A. Baldenegro-Pérez, M. Morales-Luna, T.G. Sánchez, D. Santos-Cruz, S.A. Mayén-Hernández, J. Santos-Cruz. Physical properties of photoconductive Ag–Sb–S thin films prepared by thermal evaporation. *Mater. Sci. Semicond. Proc.* **137**, 106167 (2022).
37. X. Wang, K. Kunc, I. Loa, U. Schwarz, K. Syassen. Effect of pressure on the Raman modes of antimony. *Phys. Rev. B* **74**, 134305 (2006).
38. G. Mestl, P. Ruiz, B. Delmon, H. Knözinger. Sb_2O_3/Sb_2O_4 in reducing/oxidizing environments: an in situ Raman spectroscopy study. *J. Phys. Chem.* **98**, 11276 (1994).
39. B.S. Naidu, M. Pandey, V. Sudarsan, R.K. Vatsa, R. Tewari. Photoluminescence and Raman spectroscopic investigations of morphology assisted effects in Sb_2O_3. *Chem. Phys. Lett.* **474**, 180 (2009).
40. Yu.M. Azhniuk, D. Solonenko, V.Yu. Loya, V.M. Kryshenik, V.V. Lopushansky, A. Mukherjee, A.V. Gomonnai, D.R.T. Zahn, Flexoelectric and local heating effects on CdSe nanocrystals in amorphous As_2Se_3 films. *Mater. Res. Expr.* **6**, 095913 (2019).
41. Y.M. Azhniuk, V.V. Lopushansky, V.Yu. Loya, V.M. Kryshenik, V.M. Dzhagan, A.V. Gomonnai, D.R.T. Zahn. Raman study of laser-induced formation of II–VI nanocrystals in zinc-doped As–S(Se) films. *Appl. Nanosci.* **10**, 4831 (2020).

Received 15.08.25

Ю.М. Ажнюк, А.І. Погодін, М.Й. Філеп, В.В. Лопушанський, В.М. Кришеник, В.Ю. Ізай, Л. Сатрапінський, І.М. Войнарович, О.В. Гомоннай

СТРУКТУРНЕ ТА СПЕКТРОСКОПІЧНЕ ДОСЛІДЖЕННЯ НЕЛЕГОВАНИХ І ЛЕГОВАНИХ СРІБЛОМ ПОЛІКРИСТАЛІВ Sb_2S_3

Леговані сріблом полікристали Sb_2S_3 зі вмістом срібла до 10% отримано шляхом високотемпературного синтезу. Хімічний склад зразків, визначений за даними EDX-спектроскопії, відповідає вмісту елементів у вихідній суміші при досить рівномірному розподілі елементів по поверхні зразка з незначними відхиленнями в розподілі Ag. Дані рентгенівської дифрактометрії підтвердили орторомбічну (стибніт) структуру синтезованих полікристалічних зразків Sb_2S_3 : Ag; для срібловмісних зразків також проявляється кристалічна фаза $AgSbS_2$ (β-міаргірит). Про ймовірну присутність фази $AgSbS_2$ також можуть свідчити раманівські спектри, виміряні при низькій поверхневій густині потужності лазерного опромінення $P_{\text{exc}} = 4$ кВт/см^2). Раманівські спектри при підвищеній поверхневій густині потужності опромінення ($P_{\text{exc}} = 40$ кВт/см^2) свідчать про фотоструктурні та фотохімічні перетворення, зокрема про утворення фаз Sb_2O_3 та елементного Sb внаслідок нагрівання поверхні зразка сильно сфокусованим лазерним променем.

Ключові слова: фазозмінні матеріали, дифракція рентгенівських променів, енергодисперсійна рентгенофлуоресцентна спектроскопія, раманівська спектроскопія, окиснення.